Soft Matter

PAPER

View Article Online
View Journal | View Issue

Cite this: *Soft Matter*, 2018, **14**, 9175

Stress-oscillation behaviour of semi-crystalline polymers: the case of poly(butylene succinate)†

Chaoying Wan,*[a] Ellen L. Heeley,*[b] Yutao Zhou,[a] Shifeng Wang,[c] Conor T. Cafolla,[d] Eleanor M. Crabb[b] and Darren J. Hughes[d]

Received 15th September 2018,
Accepted 31st October 2018

DOI: 10.1039/c8sm01889h

rsc.li/soft-matter-journal

Stress oscillation has been observed in a number of linear thermoplastic polymers during the cold-drawing process, where the polymers exhibit periodic self-excited oscillatory neck propagation. However, the origin of the mechanical stress oscillation process and its relationship with the crystalline morphology of the polymer are still under debate. In this work, we revisit the stress oscillation behavior by studying a semi-crystalline polyester, poly(butylene succinate) (PBS), a biodegradable polymer suitable for biomedical and packaging applications. Stress oscillation of PBS is observed when deformed at a range of elongation rates from 10 to 200 mm min^{-1}, and the fluctuation magnitude decays as the deformation temperature increases from 23 to 100 °C. Periodic transparent/opaque bands form during necking of PBS, which consists of alternating regions of highly oriented crystalline zones and microcavities due to crazing and voiding, although the degree of crystallinity did not change significantly in the bands. Simultaneous small- and wide-angle X-ray scattering confirms that the alternating stress increases, as shown in the stress–strain curves, correspond to the appearance of the transparent bands in the sample, and the abrupt drop of the stress is the result of voiding during the neck propagation. The voiding and cavitation are ultimately responsible for the stress oscillation process in PBS. The in-depth analysis of this work is important in understanding and controlling the occurrence of instabilities/cavitation during polymer processing such as film blowing, biaxial stretching and injection moulding of biodegradable polymer materials.

1. Introduction

To address global environmental issues caused by plastic wastes, biodegradable polymeric products are in high demand in order to replace oil-based plastics in many applications such as packaging and medical devices. Besides the unique biodegradability, some biodegradable polymers exhibit strong structural and test-condition dependent mechanical behaviors, which affect the properties and processing of the polymers. Plastic deformation of semi-crystalline polymers generally follows stress yielding, neck propagation and strain hardening until fracture. Following stress shearing and yielding, the polymer chains generally start to slip and orientate along the external tensile force, showing an extension of the strain at a constant stress in the process of neck propagation. Under certain testing conditions, some linear polymers exhibit unusual self-excited oscillation during the neck propagation, *i.e.*, a non-uniform necking accompanied with periodical stress fluctuation.[1–4] Stress oscillation (SO), occurs when necking is no longer constant during elongation. It can be seen in amorphous and semi-crystalline polymers during cold drawing and is characterised by obvious periodic formation of transparent and opaque banding perpendicular to the deformation direction. The SO and instability of necking have been observed in a number of thermoplastic polymers, such as amorphous polyethyleneterephthalate (aPET),[2,5–9] copolyesters,[10] high density polyethylene (HDPE),[1,11] syndiotactic polypropylene (sPP)[8,12–14] and polyamide[1,15,16] at room temperature, and polycarbonate (PC) at elevated temperatures.[17]

The SO mechanism is under debate although, it was proposed that the mechanical work was converted into thermal energy which generated local heat instability in the neck region of the polymer sample.[18] In the case of aPET, the deformation induced a local temperature rise in the neck section up to 90–140 °C, higher than its glass transition temperature (~75 °C),[19] which softened the polymer chain segments and resulted in a reduction of stress.[9] This non-isothermal process has been

[a] *International Institute of Nanocomposites Manufacturing (IINM), WMG, University of Warwick, CV4 7AL, UK. E-mail: chaoying.wan@warwick.ac.uk*
[b] *Faculty of Science, Technology, Engineering and Mathematics, Open University, Walton Hall, Milton Keynes, MK7 6AA, UK. E-mail: Ellen.Heeley@open.ac.uk*
[c] *School of Chemistry and Chemical Engineering, Shanghai Jiao Tong University, 200240, China*
[d] *WMG, University of Warwick, CV4 7AL, UK*

† Electronic supplementary information (ESI) available. See DOI: 10.1039/c8sm01889h

discussed in Barenblatt's model,[3] which is regarded as a dynamic system in a phase space of stress, drawing velocity and temperature at the neck. However, Barenblatt's model does not consider the effect of drawing rates. A simultaneous non-linear equation was further derived by Toda[7,9,20] which has provided a steady-state solution related to the stress oscillation, neck propagation velocity and temperature. Toda proposed that the effect of crystallization which occurs due to a temperature rise or high drawing rates, accounts for the self-excited SO behavior. Ebener[8] also demonstrated that the magnitude of SO is related to the tensile conditions, such as strain rate, temperature, thickness and length of polymer samples. The SO behavior was observed only when the sample length was above a critical level, and higher strain rates also promoted the magnitude of oscillation.

For semi-crystalline PET,[6] it is reported that the polymer chains orientated and bundled together under the tensile force, which led to local heat release and thus induced crystallization. The molecular bundling reduced the polymer volume and caused cavitation or micro-voiding under the constraints of drawing (shown as opaque banding). The crystallization was regarded as the origin of the SO behavior and the samples showed more than 50% cavitation.[6] The local heat did not dissipate easily through the cavities which induced the next stage of crystallization. This SO behavior observed in PET appeared as an alternative crystallization/voiding and stress increase/drop process.[6]

In this work, the self-oscillatory mechanism of linear polymers is revisited by studying the stress–strain behavior of poly(butylene succinate) (PBS), a promising biodegradable polymer that has found important applications in film blowing and fiber spinning for food packaging and biomedical devices.[21,22] PBS has comparable mechanical and processing properties as HDPE. Our recent study has revealed that the mechanical response of PBS is strongly dependent on its crystalline structure and test conditions. PBS exhibits obvious SO behavior under a range of deformation processes, which has been overlooked by most other studies.[13,23] It was recently reported that the SO behavior was only observed in PBS copolymers instead of pure PBS. Crystalline structures were detected in both the transparent and opaque bands, and a greater concentration of voiding occurred in the opaque bands compared with the transparent bands of the post-deformed SO regions. However, there is no in-depth crystalline morphology analysis of the PBS copolyester system.

The cavitation in a deformed sPP sample was confirmed by using μ-small and μ-wide-angle X-ray scattering (μSAXS/μWAXS).[13] From μSAXS, equatorial scattering around the beam stop indicated the increased cavitation in the opaque bands as well as oriented meridional peaks showing the crystalline lamellar repeat distance. Whereas, μWAXS confirmed a crystal transformation occurs in the SO bands. Moreover, no significant change in the degree of crystallinity of the transparent and opaque bands was detected suggesting that the SO does not induce crystallization and the cavitation process is the main yielding mechanism for sPP. Hence, there are various theories to account for the SO process and this would be expected to be different for the process occurring in amorphous polymers such as PC, compared with semi-crystalline polymers such as sPP.

In this work, we have carried out detailed analysis of the SO behaviour of PBS over a wide range of tensile testing conditions by using mechanical, thermal (differential scanning calorimetry, DSC), SEM and SAXS/WAXS techniques. The origin and mechanism of SO were examined by mapping the micro- and macro-morphologies, orientation of the polymer chains and crystalline lamellar stacks that have developed in the opaque and transparent bands by SAXS/WAXS analysis. The localized orientation, crazing, and fibril pulling during the necking propagation were characterized by SEM. The in-depth analysis is important in illustrating of the mechanism of SO and occurrence of instabilities/cavitation during polymer processing such as film blowing, biaxial stretching and injection molding of biodegradable polymer materials.

2. Experimental

2.1 Materials and sample preparation

PBS with melt flow index of 10 g/10 min (190 °C, 2.16 kg, T_m = 120 °C, T_g = −32 °C) was purchased from Sigma, UK. The polymer was dried in a vacuum oven at 80 °C for 24 h before use. PBS was compression-moulded at 150 °C and 15 MPa for 10 min, then compressed at room temperature at 10 MPa for 15 min. The PBS was cut into dumbbell tensile samples (1 mm in thickness) according to ASTM D638.

2.2 Characterisation and testing

The tensile properties of PBS samples were tested using a universal tensile machine (Instron 3367) coupled with a temperature-controlled chamber. The stress–strain curves were recorded at a range of elongation rates between 10 and 200 mm min^{-1} and temperatures (60, 70, 90, 100 °C), with a methodology according to ASTM-D638-14 type V. The mechanical testing results were the average values of five specimens under each testing temperature.

Scanning electron microscopy imaging was carried out using a Carl Zeiss Sigma Field Emission SEM (FESEM) at 5 kV. The cryo-fractured PBS samples were sputter-coated using an Au/Pd target.

Differential scanning calorimetry (DSC) was carried out using a Mettler Toledo DSC1 STAR^e between −60 °C and 150 °C at a heating and cooling rate of 10 °C min^{-1} for three cycles. The melting point (T_m), heat of fusion (H_m) and crystallization temperature (T_c) were determined from the DSC thermograms and the degree of crystallinity (X_c, %) was calculated based on eqn (1):

$$X_c\,(\%) = \frac{\Delta H_m}{\Delta H_m^{\theta}} \times 100 \qquad (1)$$

where ΔH_m^{θ} is 200 J g^{-1}, being the enthalpy of fusion for 100% crystalline PBS[24] and ΔH_m the melting enthalpy of the sample.

2.3 Small- and wide angle (SAXS/WAXS) data analysis through the stress oscillation bands

A sample of deformed PBS that showed stress oscillation banding, was analyzed using small- and wide-angle X-ray scattering (SAXS/WAXS) measurements. The PBS sample (gauge length 17 mm), was drawn at 23 °C at a rate of 10 mm min^{-1} using an Intron 3367 tensile testing instrument.

Two-dimensional SAXS/WAXS measurements were performed on beamline I22 of the Diamond Light Source, synchrotron, UK.[25] The X-ray energy used was 12.4 keV. A sample chamber was positioned on the beamline where the sample was secured vertically by clamps in the chamber.[26] A vacuum pipe (reducing air scattering and absorption), was positioned between the sample chamber and a Pilatus P3-2M SAXS detector, at a distance of 1.97 m. A Pilatus P3-2M-DLS-L WAXS detector was positioned at a sample-to-detector distance of 162 mm. The SAXS and WAXS detectors were calibrated with silver behenate and silicon powder, respectively. The sample was moved vertically using a translation stage, at increments of 0.125 mm steps through a distance of 3.5 mm. At each increment 2D SAXS/WAXS data was obtained at an acquisition time of 1 s.

SAXS/WAXS data was normalized for sample thickness, transmission and background scattering using the DAWN[27,28] and CCP13 Fibrefix[29] data reduction software. The 2D SAXS data frames were reduced to 1D scattering profiles of intensity (I) *versus* scattering vector (q), (where $q = (4\pi/\lambda)\sin(\theta)$); 2θ being the scattering angle and λ the X-ray wavelength. Similarly, the 2D WAXS data frames were reduced to 1D scattering profiles of intensity (I) *versus* 2θ. The 1D SAXS/WAXS scattering profiles were obtained by sector integrations taken symmetrically around the pattern, with a fixed angle and radius, q. To obtain the changes in orientation of the PBS sample, radial azimuthal 1D SAXS profiles (where the angular variation in intensity, $I(q, \varphi)$, at a fixed radius q, over an azimuthal angle, φ, range of 0–360°), where taken from the 2D SAXS patterns. The two peaks in the 1D azimuthal profiles were then fitted using Lorentzian functions to obtain the average full-width half-maximum (FWHM).

Correlation function analysis was performed on the 1D SAXS profiles using Corfunc[30] incorporated into the SasView[31] software package. The correlation function, $\gamma(R)$ where R is the real space coordinate length, is expressed as:

$$\gamma(R) = \frac{1}{Q_s}\int_0^\infty I(q)q^2\cos(qR)\mathrm{d}q \quad (2)$$

where $I(q)$ is the scattering intensity and Q_s is the experimental invariant expressed as:

$$Q_s(t) = \int_0^\infty q^2 I(q)\mathrm{d}q \approx \int_{q_1}^{q_2} q^2 I(q)\mathrm{d}q \quad (3)$$

Q_s is obtained from the 1D SAXS profile scattering between the experimental limits of q_1 (first real data point) and q_2 (region where $I(q)$ is constant). Correlation functions were computed from the extrapolation of data ($q \to \infty$) according to Porod's law[32] and a back extrapolation from the Guinier model ($q \to 0$).[33] The correlation function assumes an ideal two-phase lamellar morphology[33,34] allowing parameters[30] such as long period, L_p, crystalline layer thickness L_c, amorphous layer thickness L_a and crystallinity X_c to be extracted.

3. Results and discussion

3.1 Effects of elongation rate and temperature on the tensile behavior of PBS

The stress–strain curves for PBS deformed at a range of elongation rates and a temperature of 23 °C, are shown in Fig. 1A. All samples exhibit a typical deformation behavior seen in semi-crystalline polymers, which starts from an initial elastic deformation, then stress yielding, neck propagation, strain hardening until final fracture. For most semi-crystalline polymers, the neck-propagation is a process where the polymer chains slip and orientate along the direction of deformation, causing an extension of the strain at a constant stress due to the viscoelasticity of the polymer. However, at room temperature, PBS exhibits strain hardening and a second yielding, followed by a unique stress oscillation behavior, where the neck-propagation is interrupted and follows a stop-start cycling process, corresponding to a stress drop and recovery. As a result, periodic transparent/opaque bands

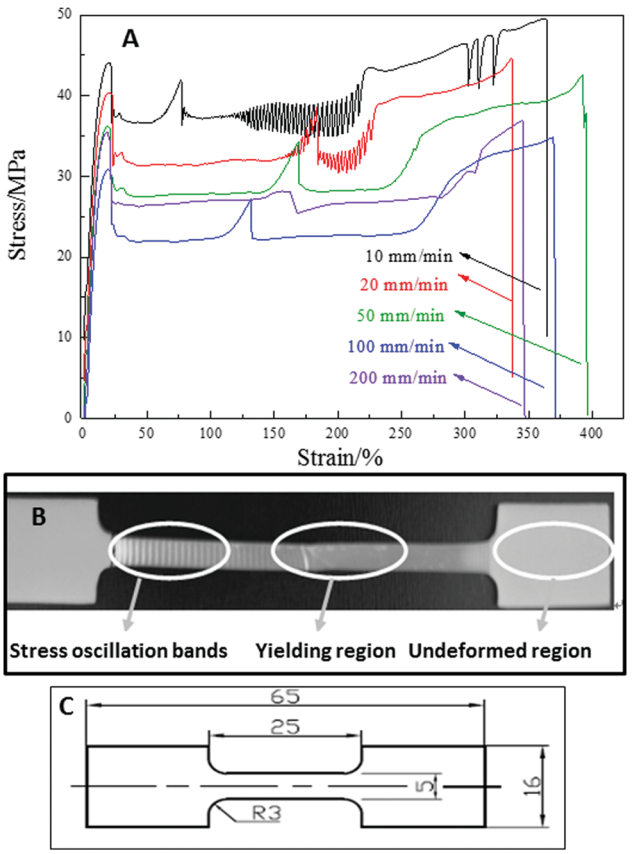

Fig. 1 (A) Tensile behavior of PBS deformed at a range of elongation rates and a temperature of 23 °C. (Data is offset vertically for clarity.) (B) A deformed PBS sample at 10 mm min^{-1} and a temperature of 23 °C, showing stress oscillation bands, yield region and undeformed region. (C) Dimensions of the tensile specimen (in mm).

are formed in the necking section of the sample, as shown in Fig. 1B. Fig. 1C shows a schematic with dimensions of the PBS dumbbell samples tested. To illustrate the stress oscillation behaviour a video clip of the process is supplied in the ESI;† the PBS is drawn at 23 °C and a rate of 10 mm min^{-1} in the video and the SO banding is seen to develop from the neck region in the sample. Similar stress oscillation has been observed in semi-crystalline syndiotactic PP,[8,12–14] polyamide[1,15,16] and copolyesters[10] under certain testing conditions, which is attributed to the local temperature increase at the neck front, orientation induced crystallization or the formation of crazes and micro-cavities.

The tensile properties of PBS at 23 °C and different testing rates are listed in Table 1. When PBS is deformed at a testing rate of 10 and 20 mm min^{-1}, the self-excited necking oscillation appears in the range of 120 to 220% of strain, with a stress magnitude of between 25 and 28 MPa. For the samples tested at a higher rates from 50 to 200 mm min^{-1}, the periodic stress oscillation is absent, where increasing the testing rate shifts the onset of the oscillations.[8] The increase in strain rate tends to reduce localized load in a certain velocity range.[5,8,9] The decrease in SO behavior only occurs where the velocity is in a critical range, heat dissipation occurs and hence softening of the polymer, excess heat dissipation at high strain rates increases further and thus softening increases and SO attenuates, which has been observed in PET and sPP polymers.[8,9]

In PBS, a second yielding appears independent of the elongation rate. The double-yielding behavior has been observed in isotactic PP[35] and polyamide.[36] In the case of semi-crystalline PBS with a T_g of ~−32 °C, the second yielding may be caused by the partial melting-recrystallization process.[35,37,38] The locally concentrated uniaxial stress may cause fusion of the less perfect crystallites, and then induce recrystallization along the drawing direction. It is not necessary for a large temperature increase to take place in order for partial melting to occur and the melted species to recrystallize.[37,38]

To study the effects of temperature on the stress oscillation of PBS, the samples were deformed at 10 mm min^{-1} under a range of temperatures from 23 to 100 °C. The stress–strain curves are shown in Fig. 2 and tensile properties are collated in Table 2. The tensile yield strength of PBS was seen to decrease with increasing deformation temperature and the elongation at break increased accordingly. Higher temperatures of 60–70 °C induced an initial start of intensive stress oscillation right after yielding until a strain of 150%, then followed by a periodic oscillation until fracture. This indicates that the higher temperature allows the PBS chains to move more freely (PBS T_g −32 °C)

Table 1 Tensile properties of PBS drawn at different rates at a temperature of 23 °C

Tensile rate/ mm min^{-1} (at 23 °C)	Yield strength/MPa	Elongation at break/%	Young's modulus/MPa
10	33.5 ± 1.3	361 ± 18	288 ± 12
20	34.0 ± 1.4	357 ± 22	310 ± 21
50	34.6 ± 2.0	393 ± 28	299 ± 24
100	35.0 ± 1.9	355 ± 23	305 ± 33
200	35.5 ± 2.1	346 ± 35	315 ± 26

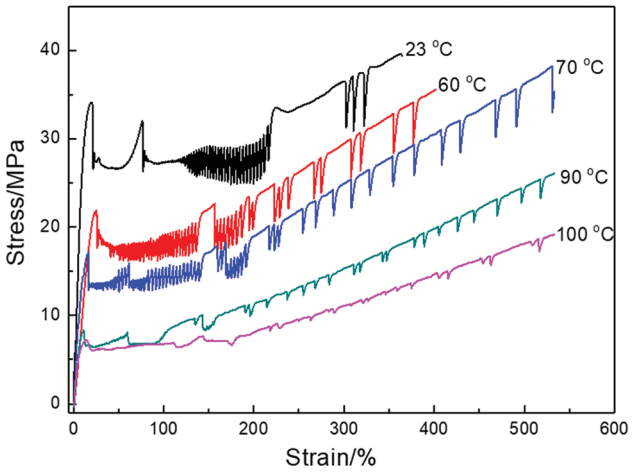

Fig. 2 Tensile behavior of PBS deformed at 10 mm min^{-1} and various temperatures. (Data is offset vertically for clarity.)

Table 2 Tensile properties of PBS drawn at different temperatures and a rate of 10 mm min^{-1}

Tensile temperature/ °C (at 10 mm min^{-1})	Yield strength/ MPa	Elongation at break/%	Young's modulus/MPa
23	33.5 ± 1.3	361 ± 18	288 ± 12
60	21.8 ± 2.0	405 ± 23	120 ± 19
70	17.1 ± 2.1	532 ± 35	122 ± 15
90	8.3 ± 1.1	533 ± 26	113 ± 12
100	7.2 ± 1.2	536 ± 27	113 ± 16

and slows down the dissipation of the localized heat from the sample, therefore promoting the initial start of stress oscillation. When PBS was deformed at 90–100 °C, the stress oscillation still appeared but was much weaker. At higher draw temperatures elongation proceeds without the formation of a necking region which has been observed in PBS,[39] where the molecular chains have greater mobility, and the SO amplitude reduces and attenuates as the sample flows more homogeneously.[5,8]

3.2 Thermal analysis of deformed PBS

Fig. 3 shows the DSC thermograms for different sections of a deformed PBS sample (tensile testing at 10 mm min^{-1} and a temperature of 23 °C). A small exothermic crystallization peak was observed at 95 °C in the original PBS sample, but was absent in the stretched samples. This peak is ascribed to the recrystallization and perfection of crystallites with low thermal stability.[24,39–41] The melting peak occurs at ~114 °C for all the PBS samples, thus the formation of the stress oscillation bands did not affect the T_m. However, the degree of crystallinity of PBS increased from 29.5% to 35% after cold-drawing, indicating the occurrence of strain-induced crystallization. The thermal properties of the yielding section and the stress oscillation section are similar and shown in Table 3. Similar observations were reported from the DSC analysis of sPP[11] for the stress oscillation bands, where the increase in crystallinity in the banding was attributed to the orientation and thus strain-induced crystallization during deformation.

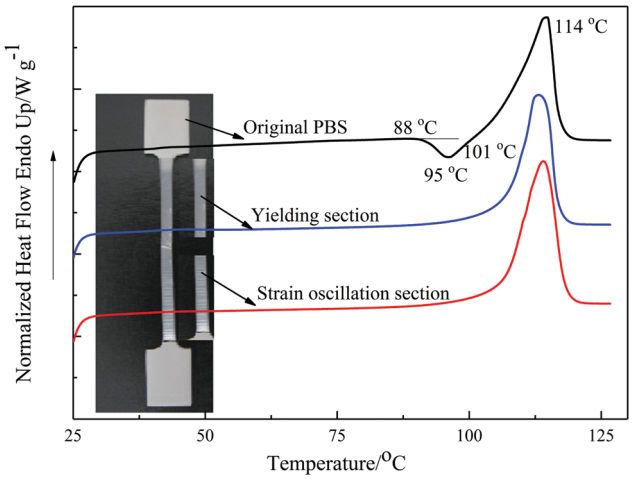

Fig. 3 The first heating DSC thermograms of different sections of drawn PBS deformed at 10 mm min^{-1} and a temperature of 23 °C.

Table 3 Thermal parameters of drawn PBS deformed at 10 mm min^{-1} and a temperature of 23 °C

Sample	ΔH/J g^{-1}	T_m/°C	X_c/%
Undeformed	59.0	114.0	29.5
Yielding	71.2	114.5	35.6
SO region	70.0	114.1	35.0

Fig. 4 shows the first DSC heating and cooling thermograms for PBS deformed at 10 mm min^{-1} at different drawing temperatures, taken from the yielding region. The thermal parameters are collected in Table 4. The degree of crystallinity of PBS at the yielding region, increased with increasing deformation temperatures from 23 to 70 °C, and then decreased when the deformation temperature was above 70 °C. This corresponds to the stress–strain curves in Fig. 2, the deformation temperature below 70 °C facilitates the strain-induced crystallization. When the temperature is above 70 °C, the deformation is mainly caused by the alignment and movement of the polymer chains, and the stress oscillation mainly arises from the craze formation. The value of T_m increases with increasing draw temperature, as does T_c, which can be attributed to the alignment of the molecular chains into ordered bundles with elongation. These oriented chain bundles can act as nucleation points for small crystallites to form and increase T_m. These oriented bundles can persist in the melt which provide nucleation sites for crystallites on cooling, so T_c increases as well.

3.3 Surface morphology of the SO bands in PBS

The cross sections of the SO bands of PBS were observed by SEM, the results are shown in Fig. 5. For semi-crystalline polymers, tensile processing can induce crystalline regions to re-stack and amorphous region to crystallize. Fig. 5A, shows the PBS sample deformed at 20 mm min^{-1} and 23 °C, displaying clear alternating stress oscillation bands. Fig. 5B details the side view of the magnified transparent section of the sample. In Fig. 5C, three modes of fracture are observed in the periodic bands; the micro-voids being formed

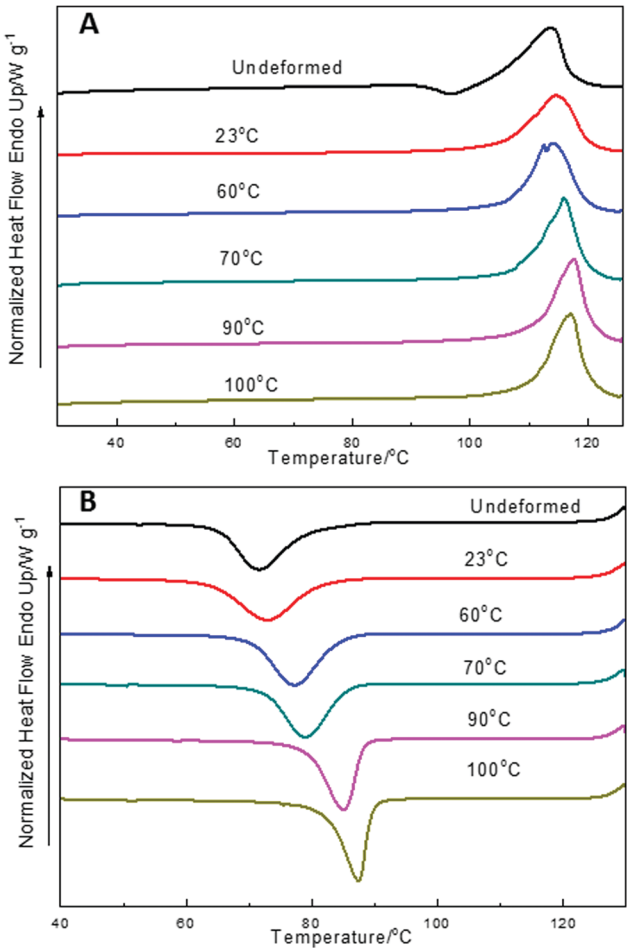

Fig. 4 DSC thermograms of PBS deformed at 10 mm min^{-1} and different draw temperatures. (A) First heating cycle; (B) the following cooling cycle.

Table 4 Thermal parameters of PBS at different tensile testing temperatures

Tensile testing temperature/°C	ΔH/J g^{-1}	T_m/°C	X_c/%
Undeformed PBS	59	114.0	29.5
23	71.2	114.5	35.6
60	77.5	114.1	38.7
70	79.9	115.9	39.9
90	75.5	117.5	37.7
100	74.3	117.0	37.1

in between microfibrils; the pull-out of the fibrils and crazing, which finally resulted in cavitation. This explains the fluctuations of necking and induces the periodic changes of its appearance in the form of transparent/opaque bands in the deformed sample (Fig. 5A).

Similar observations were reported in PET[42] where the cavitation formed inside of the samples. At a certain strain rate, the aPET chains were sheared and orientated, creating fiber bundles and crazes. The formation of the crazes and cavities reduced the thermal conductivity of the polymer, as a result, local heating occurred in the deformation zone (36–40 °C) and caused the decrease of the strength and elongation. During the necking, the heat was dissipated, cooling down the polymer, which

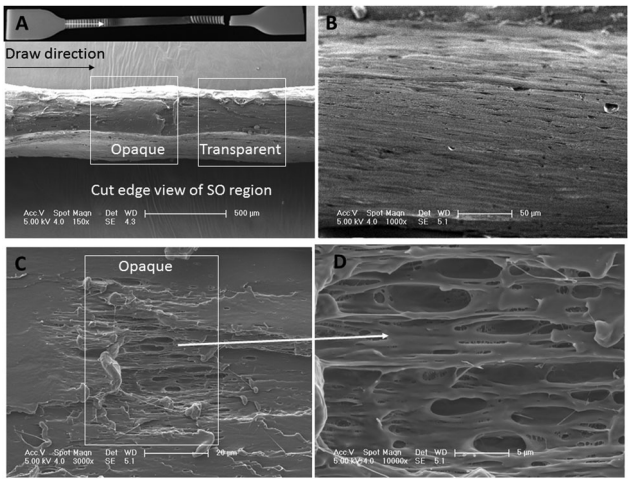

Fig. 5 SEM images of fracture surface of PBS drawn at 20 mm min^{-1} and 23 °C. (A) Edge view of cut opaque and transparent SO bands (inset shows the tested sample with alternating necking and SO bands); (B) higher magnification image of the transparent band of A; (C and D) showing cavities and voiding in the opaque band.

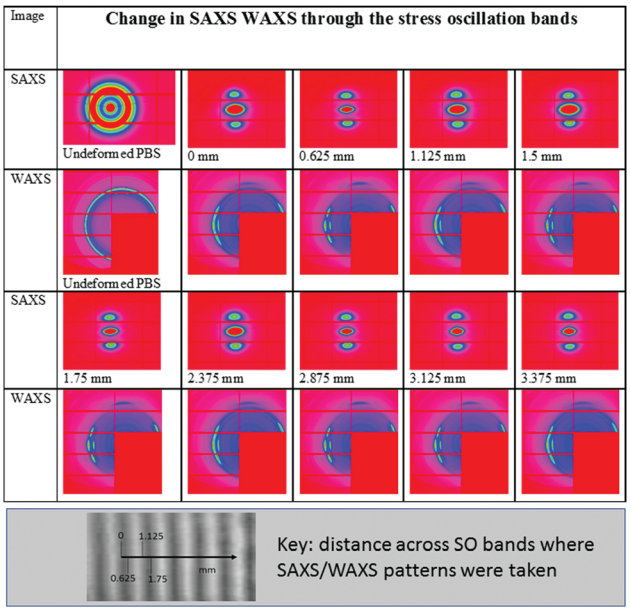

Fig. 6 Simultaneous 2D SAXS/WAXS patterns of undeformed PBS and those obtained moving through the stress oscillation bands (see key for distance across sample). The deformation direction is vertical in all patterns. (SAXS – beam stop is in the centre of the pattern; WAXS beam stop is excluded as occurs in the red rectangle of the pattern where the detector modules are absent.)

caused an increase of the strength. The cycling of this process resulted the periodic oscillation of the stress. A banding structure was observed in PBS copolyesters during tensile deformation,[23] where greater voiding and cavitation occurred in the opaque band. Fibril structures parallel to the deformation direction occurred in both the opaque and transparent bands, but in greater concentration in the transparent bands.

3.4 Micro- and macro-morphology of the SO bands in PBS

Closer inspection of the SO bands was performed using SAXS/WAXS to give an insight into the micro- and macro-crystalline morphology and orientation across the SO banding of a pre-deformed sample drawn at 23 °C and a rate of 10 mm min^{-1}. Simultaneous 2D SAXS/WAXS patterns were obtained (at a step distance of 0.125 mm) through the sample where position 0 mm represents the edge of the opaque–transparent band (see key in Fig. 6). Fig. 6 shows the 2D SAXS/WAXS patterns of undeformed PBS; SAXS shows a characteristic sharp ring of intensity (around the central beam stop), indicating a randomly oriented lamellar morphology is present before deformation. The 2D WAXS shows sharp intense Bragg rings, indicating the crystalline nature of the undeformed PBS. Once deformed the 2D SAXS patterns show two features; intense scattering around the beam stop which is slightly elongated in the equatorial direction (perpendicular to the deformation direction), and sharp spots on the meridian (parallel to the deformation direction). The sharp meridional spots indicate that throughout the SO bands, the lamellar morphology (or lamellar stacking) is now well oriented in the deformation direction.[43,44] The 2D WAXS also shows the Bragg rings have now concentrated into sharper arcs and spots on the equator, again confirming a highly oriented crystalline morphology. Returning to the 2D SAXS equatorial scattering around the beam stop; the size and intensity changes through the SO bands. This scattering is attributed to the voiding and crazing in the SO bands, which is greater in the opaque bands (see Fig. 5), than in the transparent bands. One observation to note is that the equatorial scattering does not show any sharp streaks in this direction which would indicate the formation of bundles of highly oriented molecular chains aligning parallel to the direction of deformation.[44–46] Similar observations of equatorial SAXS scattering were made across the SO bands in sPP by García Gutiérrez *et al.*,[13] whereby they proposed that the voiding and crazing was the main yielding mechanism due to the absence of equatorial SAXS streaks.

To confirm the changes in the equatorial SAXS scattering through the SO bands, the integrated equatorial scattering was computed with distance. The change in equatorial scattering is shown in Fig. 7, including the SAXS patterns at the peak and trough positions on the equatorial intensity plot.

The change in the equatorial scattering profile with distance is remarkably analogous to the stress oscillations shown in the tensile stress–strain curves. The 2D SAXS indicates that at the peak SO positions there is greater scattering around the beam stop caused by voiding, which decreases sharply towards the troughs on the intensity plot. This confirms the development of the opaque bands (where light scattering is caused by the crazing and voiding) and increased scattering around the beam stop. This scattering intensity then reduces when crossing into the transparent band, where the scattering around the beam stop decreases, as there is less voiding/crazing in the sample in this region.

Fig. 8 shows an example of the expanded view of the 2D WAXS patterns at two positions across the SO bands; the position 0 mm represents the edge of the opaque band and the position 0.625 mm is in the transparent band. Bragg reflections observed

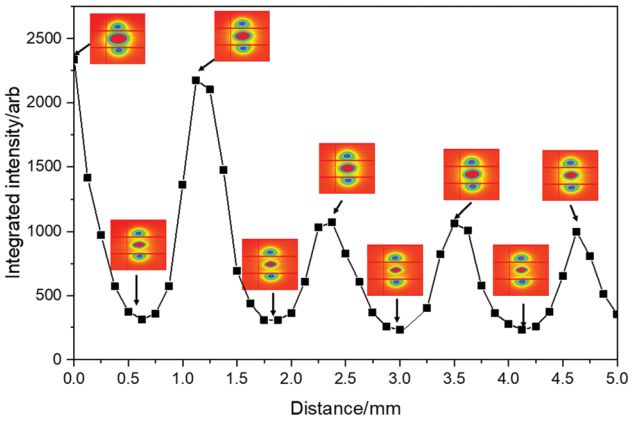

Fig. 7 Integrated equatorial intensity across the SO bands. Corresponding 2D SAXS patterns are given at peaks and troughs on the integrated intensity plot.

relate to the monoclinic α form unit cell crystal lattice, where the main peaks indexed as (020), (021) and (110) are labelled.[47] The spots sharpen on the equator travelling through the SO bands due to increasing crystallite orientation and perfection.

The 1D WAXS data (obtained from the 2D WAXS patterns) through the SO bands are shown in Fig. 9, where the (020), (021) and (110) peaks are labelled. During deformation, PBS often undergoes a crystal transition from the α to the β crystal form, which is indicated by the emergence of other WAXS peaks[39,48–50] (the $(120)_\beta$, $(021)_\beta$ and $(002)_\beta$ reflections), however, no extra peaks were seen to emerge in the WAXS patterns here, therefore no crystal transition occurred under the deformation conditions applied.

Further analysis was performed on the SAXS data to obtain quantitative information about the change in the orientation of the lamellar stacks, long period and crystallinity during the SO process. The FWHM was obtained from azimuthal profiles of the 2D SAXS patterns. Fig. 10A and B, shows a selection of the 1D azimuthal profiles obtained from the 2D SAXS data and change in FWHM, across the SO bands, respectively.

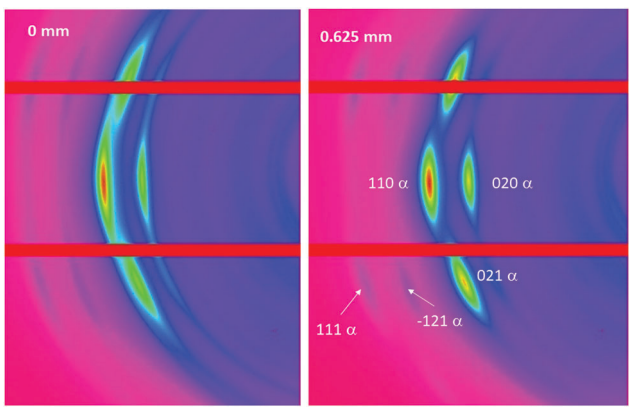

Fig. 8 Expanded 2D WAXS patterns showing the monoclinic α form of the PBS unit cell including indexed peaks, at two positions (0 mm and 0.625 mm) across the SO bands.

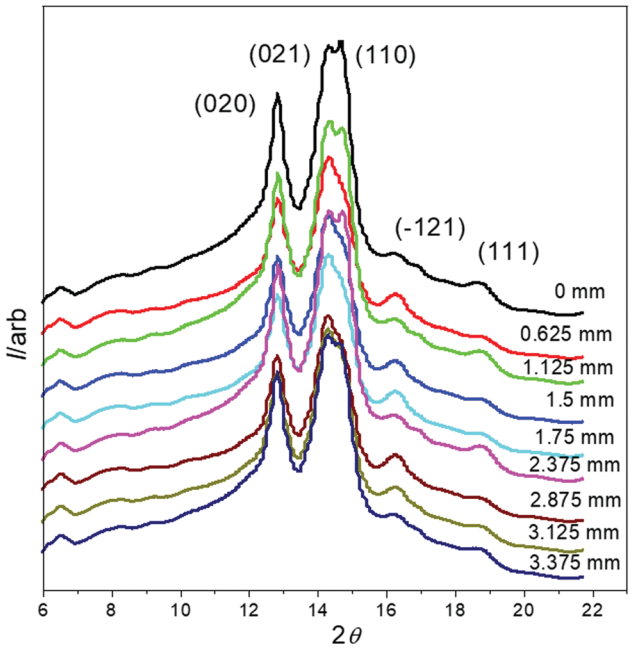

Fig. 9 1D WAXS data of PBS across the SO bands (data off-set on the vertical axis for clarity).

The 1D SAXS azimuthal profiles in Fig. 10A, show sharp well-defined peaks which were fitted to obtain the FWHM across the SO bands. The change in FWHM (Fig. 10B), again shows

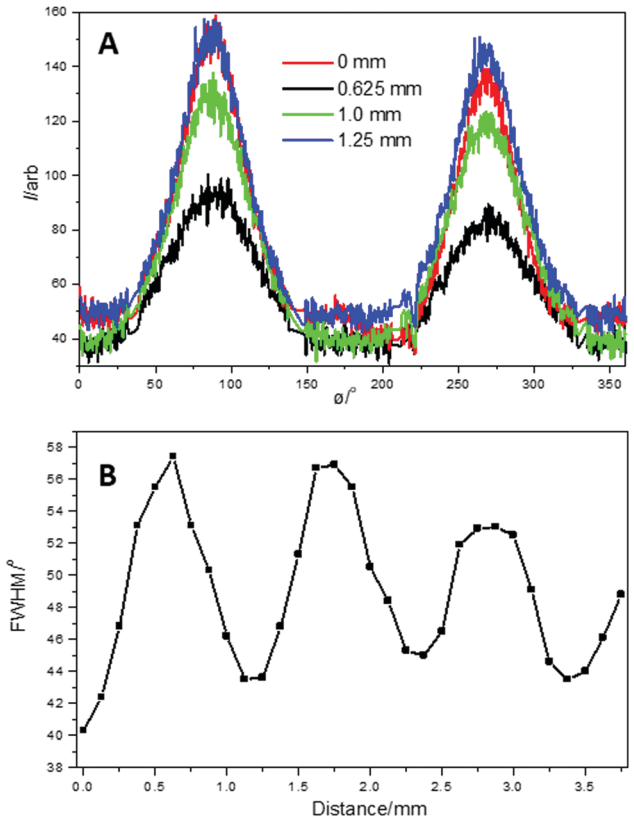

Fig. 10 (A) Example 1D SAXS azimuthal profiles obtained from the 2D SAXS data; (B) change in FWHM through the SO bands.

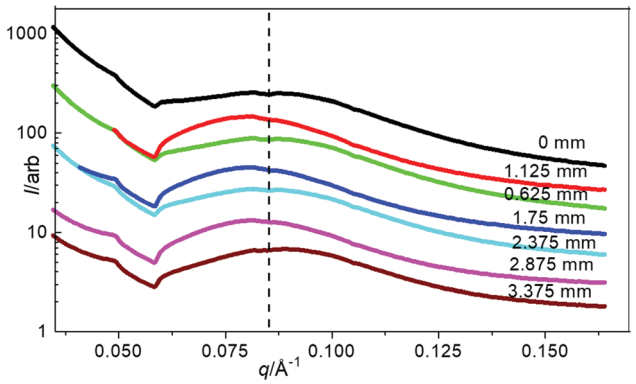

Fig. 11 1D SAXS profiles showing the change in peak position across the SO bands.

comparable oscillations to both the tensile extension curve (Fig. 6) and the change in the integrated equatorial intensity (Fig. 8). Therefore, the orientation of the lamellar stacks (representing a long-rage ordering), follows the stress oscillation, where the increasing FWHM indicates a decrease in lamellar stack orientation and *vice versa*.

The 1D SAXS profiles obtained from sector integrations of the 2D SAXS patterns are shown in Fig. 11. The maximum peak position indicates the average long period of the lamellar stacks (average length scale of the amorphous and crystalline layers), which shifts slightly across the stress oscillation bands. The most oriented lamellar stack position (from FWHM) has a smaller long period (positioned at higher $q \sim 0.087$ Å^{-1}) which shifts to a larger long period (positioned at lower $q \sim 0.080$ Å^{-1}), at the least oriented lamellar stack position. The peak position oscillates around an average of 0.084 Å^{-1}. To determine a more quantitative analysis of the 1D SAXS profiles in Fig. 12, 1D correlation functions were computed, where the long period, L_p, crystalline L_c and amorphous L_a layers and crystallinity are extracted (Fig. 12).

Fig. 12A shows an example of the computed correlation functions for the undeformed and deformed PBS sample from the 1D SAXS profiles. The second peak maxima gives the long period L_p, which is 71 Å for the undeformed PBS, and 60 Å for the deformed PBS. The reduced L_p caused by the deformation could be due to the breaking up and orientation of the random lamellar structure under strain. The change in L_p across the SO bands is shown in Fig. 12B. Here, once again the change in L_p shows a similar pattern of SO as the mechanical profiles and FWHM (Fig. 10), rising from 60 Å to 68 Å, and then falling to ~60 Å, once again. In Fig. 12C, the change in crystalline (L_c) and amorphous layer (L_a) thickness is shown across the SO bands. It should be noted that $L_c + L_a = L_p$ from the correlation function analysis.

Generally, the L_a increases and decreases with the oscillation that matches the change in L_p. This indicates that the increase in the L_p is matched to the increase in L_a and correspondingly to a small decrease in L_c. This is mirrored in Fig. 12D, where the change in bulk crystallinity (X_c) across the SO bands is plotted. There is a reduction in X_c which corresponds to the reduction in crystalline layer thickness.

To interpret the deformation and then SO process in PBS (during cold drawing) and correlate this with the observations

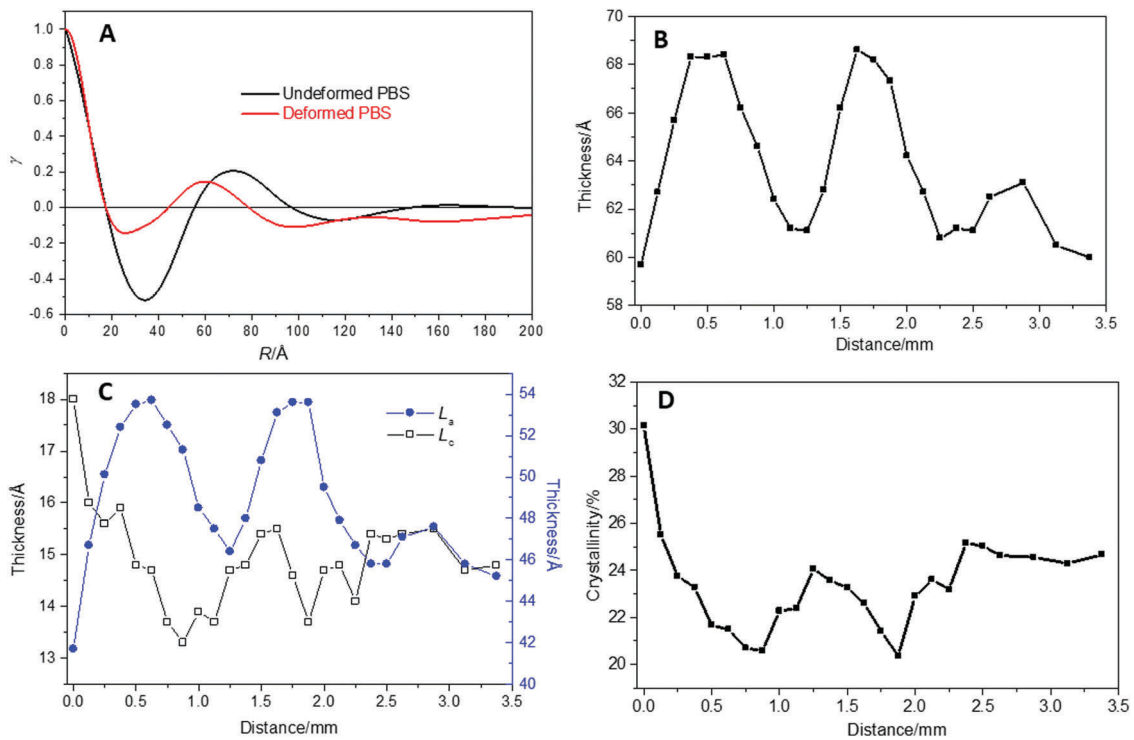

Fig. 12 (A) Example correlation function for undeformed PBS and deformed PBS, computed from the 1D SAXS profiles. (B) Change in long period; (C) change in crystalline and amorphous layer thickness and (D) change in crystallinity, across the SO bands.

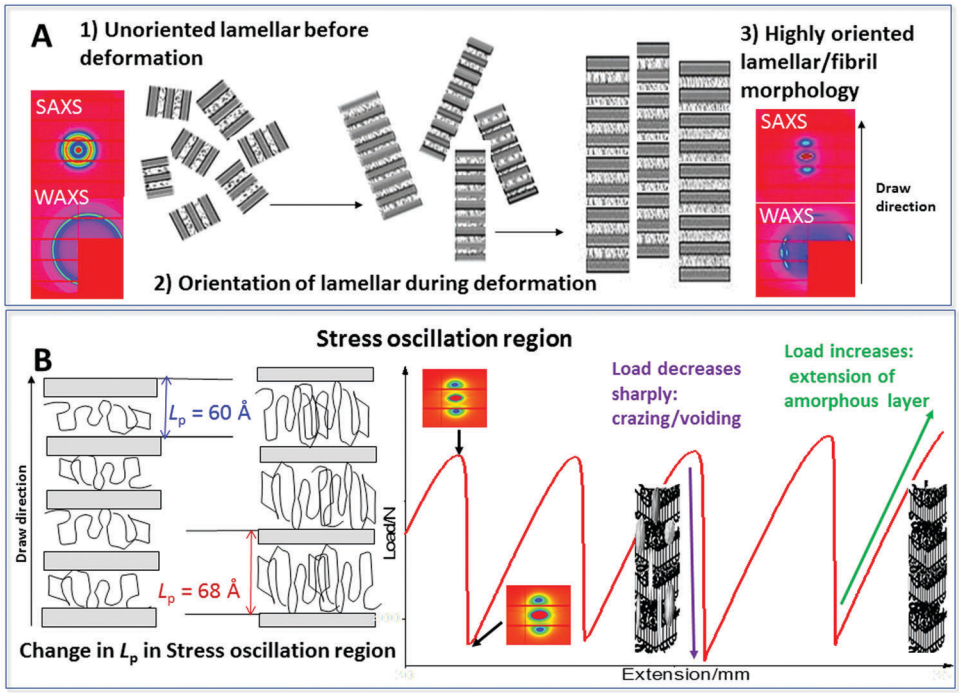

Fig. 13 (A) Deformation changes in PBS initially with as unoriented lamellar morphology with corresponding SAXS/WAXS patterns. As the PBS is deformed the lamellar structure orients in the draw direction. A highly oriented lamellar/fibril morphology is produced with corresponding SAXS/WAXS patterns. (B) Stress oscillation region during continued deformation – change in L_p mirrors the SO curve. The load sharply decreases as crazes and voids occur in the PBS, the load then increases as the amorphous layer is extended.

found in SAXS/WAXS data, we present the schematic in Fig. 13. In Fig. 13A, the initial crystalline unoriented lamellar structure is observed in the undeformed material, which is confirmed by the unoriented SAXS/WAXS patterns. As the PBS is deformed the lamellar structure orients in the draw direction and a highly oriented lamellar/fibril morphology is produced again confirmed by the oriented nature of the SAXS/WAXS patterns.

Fig. 13B, depicts the SO region of the deformation process. The L_p is seen to oscillate in a similar manner to the mechanical profile. During elongation, local heating occurs at the neck front which softens the polymer and the molecular chains become mobile. The amorphous chain regions and tie chains linking the lamellar crystallites extend. At the maximum in the SO profile the lamellar crystallites are pulled apart under the strain and this then results in cavitation/voiding in the sample. The occurrence of the cavitation and voiding causes a sudden decrease in the stress. The voiding is seen in the 2D SAXS patterns as increased scattering around the beam stop. The heat is not easily dissipated in the cavity's so builds and again heats the polymer chains at the neck front mobilizing the molecular chains and elongation occurs once again and the cycle is repeated. From this data the SO process producing transparent and opaque banding is correlated to localized heating, elongation and then voiding, whereby the voiding is responsible for the load drop in the mechanical profile. This observation was also seen during the deformation of semi-crystalline sPP.[13,14]

The physical and mechanical analysis here has enabled us to review and confirm the stress oscillation process in PBS, under various test conditions. The mechanical stress oscillation process can be directly correlated with a periodic change in the orientation and long-range ordering of the crystalline lamellar structure as well clarifying the formation of cavitation and voiding. The in-depth analysis of this work is important in understanding and controlling the occurrence of instabilities/cavitation during polymer processing such as film blowing, biaxial stretching and injection moulding of biodegradable polymer materials.

4. Conclusions

The origin and mechanism of stress oscillation behaviour of a semi-crystalline biopolymer PBS was examined by relating to the micro- and macro-morphologies and crystallinity to a range of testing conditions, using mechanical, thermal, SEM and SAXS/WAXS techniques. Periodic stress oscillation during the neck-propagation of PBS was observed during uniaxial tensile testing, which was dependent on the testing rate and temperature. The amplitude of stress oscillation decreased at higher tensile rates above 50 mm min^{-1}, and at temperatures above the crystalline temperature (72 °C). The crystal structure of PBS was not changed during the tensile process as illustrated by DSC and SAXS/WAXS, but the degree of bulk crystallinity was increased by 21% compared with the undeformed polymer. Microfibrils and crazes were formed and led to microcavities in the neck section, which induced the emergence of opaque regions and reduced stress in the mechanical profile. As a result,

voiding and cavitation are mainly responsible for the stress oscillation and the formation of periodic transparent/opaque bands in PBS.

Conflicts of interest

There are no conflicts to declare.

Acknowledgements

X-ray beam time at Diamond Light Source was provided under the experimental application SM-13815. We are grateful for the assistance of all the Diamond I22 beamline staff.

References

1 S. Bazhenov, Y. A. Rodionova and A. Kechekyan, *Polym. Sci., Ser. A*, 2003, **45**, 635–639.
2 G. Andrianova, A. Kechekyan and V. Kargin, *J. Polym. Sci., Part A-2*, 1971, **9**, 1919–1933.
3 G. Barenblatt, *Bull. Russ. Acad. Sci.*, 1970, **5**, 110–118.
4 D. Mouzakis, G. Kandilioti, S. Tzavalas and V. Gregoriou, *Fracture of Nano and Engineering Materials and Structures*, Springer, 2006, pp. 1285–1286.
5 T. Pakula and E. Fischer, *J. Polym. Sci., Polym. Phys. Ed.*, 1981, **19**, 1705–1726.
6 F. Ronkay and T. Czigány, *Polym. Bull.*, 2006, **57**, 989–998.
7 A. Toda, *Polymer*, 1993, **34**, 2306–2314.
8 H. Ebener, B. Pleuger and J. Petermann, *J. Appl. Polym. Sci.*, 1999, **71**, 813–817.
9 A. Toda, C. Tomita, M. Hikosaka, Y. Hibino, H. Miyaji, C. Nonomura, T. Suzuki and H. Ishihara, *Polymer*, 2002, **43**, 947–951.
10 J. Karger-Kocsis, T. Czigány and E. Moskala, *Polym. Eng. Sci.*, 1999, **39**, 1404–1411.
11 D. Mouzakis and J. Karger-Kocsis, *J. Appl. Polym. Sci.*, 1998, **68**, 561–569.
12 D. Mouzakis, *eXPRESS Polym. Lett.*, 2010, **4**, 244–251.
13 M. G. a. Gutiérrez, J. Karger-Kocsis and C. Riekel, *Chem. Phys. Lett.*, 2004, **398**, 6–10.
14 J. Karger-Kocsis and P. Shang, *J. Therm. Anal. Calorim.*, 2002, **69**, 499–507.
15 D. Hookway, *J. Text. Inst., Proc.*, 1958, **49**, P292–P316.
16 C. Hopmann, J. Klein and M. Schöngart, *AIP Conf. Proc.*, 2017, **1914**, 090004.
17 D. Chiang, M. L. Tsai and S. Lee, *Polym. Eng. Sci.*, 2013, **53**, 589–596.
18 S. Bazhenov, *Mech. Solids*, 2014, **49**, 596–603.
19 S. Bazhenov, *J. Appl. Polym. Sci.*, 2011, **119**, 654–661.
20 A. Toda, *Polymer*, 1994, **35**, 3638–3642.
21 M. Gigli, M. Fabbri, N. Lotti, R. Gamberini, B. Rimini and A. Munari, *Eur. Polym. J.*, 2016, **75**, 431–460.
22 J. Xu and B. H. Guo, *Biotechnol. J.*, 2010, **5**, 1149–1163.
23 T. Wan, J. Zhang, S. Liao and T. Du, *Polym. Eng. Sci.*, 2015, **55**, 966–974.
24 T. Miyata and T. Masuko, *Polymer*, 1998, **39**, 1399–1404.
25 Beamline-Soft Condenced Matter – Small Angle Scattering. http://www.diamond.ac.uk/Beamlines/Soft-Condensed-Matter/small-angle/I22.html, accessed 14 September 2018.
26 D. Hughes, A. Mahendrasingam, C. Martin, W. Oatway, E. Heeley, S. Bingham and W. Fuller, *Rev. Sci. Instrum.*, 1999, **70**, 4051–4054.
27 M. Basham, J. Filik, M. T. Wharmby, P. C. Chang, B. El Kassaby, M. Gerring, J. Aishima, K. Levik, B. C. Pulford and I. Sikharulidze, *J. Synchrotron Radiat.*, 2015, **22**, 853–858.
28 J. Filik, A. Ashton, P. Chang, P. Chater, S. Day, M. Drakopoulos, M. Gerring, M. Hart, O. Magdysyuk and S. Michalik, *J. Appl. Crystallogr.*, 2017, **50**, 959–966.
29 FibreFix. http://www.diamond.ac.uk/Beamlines/Soft-Condensed-Matter/small-angle/SAXS-Software/CCP13/FibreFix.html, accessed 14 September 2018.
30 A. J. Ryan, *Fibre Diffraction Review*, 1994, **3**, 25–29.
31 SasView for Small Angle Scattering Analysis. http://www.sasview.org/, accessed 14 september 2018.
32 G. Porod, *Kolloid-Z.*, 1951, **124**, 83–114.
33 F. Balta-Calleja and C. Vonk, *X-ray scattering of synthetic polymers*, Elsevier Science Ltd, 1989.
34 G. Strobl and M. Schneider, *J. Polym. Sci., Polym. Phys. Ed.*, 1980, **18**, 1343–1359.
35 T. Wu, Y. Cao, F. Yang and M. Xiang, *Mater. Des.*, 2014, **60**, 153–163.
36 G.-F. Shan, W. Yang, M.-B. Yang, B.-H. Xie, Z.-M. Li and J.-M. Feng, *Polym. Test.*, 2006, **25**, 452–459.
37 P. J. Flory and D. Y. Yoon, *Nature*, 1978, **272**, 226.
38 J. C. Lucas, M. D. Failla, F. L. Smith, L. Mandelkern and A. J. Peacock, *Polym. Eng. Sci.*, 1995, **35**, 1117–1123.
39 G. Liu, L. Zheng, X. Zhang, C. Li, S. Jiang and D. Wang, *Macromolecules*, 2012, **45**, 5487–5493.
40 Z. Qiu, M. Komura, T. Ikehara and T. Nishi, *Polymer*, 2003, **44**, 7781–7785.
41 X. Wang, J. Zhou and L. Li, *Eur. Polym. J.*, 2007, **43**, 3163–3170.
42 L. Vas, F. Ronkay and T. Czigány, *eXPRESS Polym. Lett.*, 2009, **3**, 63–69.
43 S. Röber, P. Bösecke and H. Zachmann, *Makromol. Chem., Macromol. Symp.*, 1998, **15**, 295–310.
44 E. Heeley, T. Gough, D. Hughes, W. Bras, J. Rieger and A. Ryan, *Polymer*, 2013, **54**, 6580–6588.
45 J. Schultz, B. S. Hsiao and J. Samon, *Polymer*, 2000, **41**, 8887–8895.
46 R. Kolb, S. Seifert, N. Stribeck and H. Zachmann, *Polymer*, 2000, **41**, 1497–1505.
47 K. Ihn, E. Yoo and S. Im, *Macromolecules*, 1995, **28**, 2460–2464.
48 Y. Ichikawa, J. Suzuki, J. Washiyama, Y. Moteki, K. Noguchi and K. Okuyama, *Polymer*, 1994, **35**, 3338–3339.
49 Y. Ichikawa, J. Washiyama, Y. Moteki, K. Noguchi and K. Okuyama, *Polym. J.*, 1995, **27**, 1230.
50 G. Liu, L. Zheng, X. Zhang, C. Li and D. Wang, *Macromolecules*, 2014, **47**, 7533–7539.

